

Wind in Weak Grids: Low-Frequency Oscillations, Subsynchronous Oscillations, and Torsional Interactions

Yin Li, *Student Member, IEEE*, Lingling Fan, *Senior Member, IEEE*, Zhixin Miao, *Senior Member, IEEE*

Abstract—Oscillations have been observed in wind farms with weak grid interconnections. While Texas observes 4 Hz low-frequency oscillations, the west region in China observes subsynchronous oscillations at 30 Hz. Further, this oscillation mode caused torsional interactions with a remote synchronous generator and led to shutdown of the power plant. Inspired by those real-world events, this paper aims to present an analytical model of type-4 wind in weak grids that can demonstrate both low-frequency and subsynchronous frequency oscillations. Critical factors, e.g., the parameters of the phase-locked loop (PLL), are examined using small-signal analysis. The analysis results are validated using a testbed built in MATLAB/SimPowerSystems. Except power electronic switching sequences, the testbed has controls (e.g., wind turbine pitch control, maximum power point control, converter controls), machine dynamics and power system dynamics modeled. This testbed includes a 100 MW Type-4 wind farm, a 600 MW synchronous generator, a long transmission line and a grid. The testbed successfully demonstrates two types of dominant oscillations under different PLLs. In addition, the testbed demonstrates torsional interactions due to the proximity of the subsynchronous mode and one of the torsional modes.

Index Terms—Type-4 wind, phase-locked loop (PLL), torsional interaction, low-frequency oscillations, subsynchronous oscillations.

I. INTRODUCTION

Stability issues have been reported in the literature for voltage source converters (VSCs) with weak ac grid interconnections [1]–[5], [5]–[8]. In real-world, both low-frequency oscillations and subsynchronous oscillations have been observed for wind with weak grid interconnection. While Texas observes 4 Hz low-frequency oscillations [9], the west region in China observes subsynchronous oscillations at 30 Hz [10]. This oscillation mode then caused torsional interactions with a remote synchronous generator and led to the shut down of the power plant.

Inspired by those real-world events, this paper aims to present a dynamic model that can capture essential dynamics and demonstrate the low-frequency and subsynchronous frequency oscillations. For the subsynchronous oscillations, we also aim to demonstrate its effect on torsional interactions with a synchronous generator. The demonstration will be carried out in a tested shown in Fig. 1, which consists of a type-4 wind farm and a synchronous generator. This system will be modeled in MATLAB/SimPowerSystems to demonstrate torsional interactions.

Though [10] has provided an analytical model to demonstrate subsynchronous oscillations in type-4 with weak grid interconnection, low-frequency oscillation is not in the study scope. It is of practical interest to investigate why Texas sees 4 Hz oscillations while the west China region sees 30 Hz oscillations.

In the literature, two types controls related to the d -axis grid-side converter (GSC) vector control are presented: active power control or dc-link voltage control. While investigation on HVDC with weak grid connection [4], [11] assumes active power control, investigation on type-4 wind weak grid interconnection [10], [12] assumes dc-link voltage control. In the first category, dc-link dynamics are not modeled. This assumption is also adopted in [13] on type-4 wind weak grid interconnection modeling. In the second category [10], [12], dc-link voltage control is assumed for the d -axis vector control and dc-link dynamics are modeled.

In the first category with power control mode assumption [4], [11], [13], research results indicate that only one oscillation mode with frequency less than 10 Hz is associated with weak grid. In the second category, [12] adopts frequency-domain analysis and demonstrates subsynchronous-frequency mode that can cause torsional interaction with a synchronous generator. [10] carries out eigenvalue analysis and identifies an unstable subsynchronous-frequency mode at 30.76 Hz and a low-frequency mode with large damping at 2.75 Hz. The participation factor analysis in [10] focuses on the 30.76 Hz mode only and indicates that the dc-link capacitor dynamics is related to the subsynchronous-frequency mode.

By comparing the two control mode assumptions, we discovered that both low-frequency and subsynchronous-frequency oscillation modes exist in type-4 wind with weak grid interconnection if dc-link voltage control mode is assumed. Further, PLL with a low bandwidth makes the low-frequency oscillation mode dominant while PLL with a high bandwidth makes the subsynchronous mode dominant. The analysis results have been published in a letter [14].

The PLL adopted in [14] and also this paper is synchronous reference frame (SRF)-based PLL. This type of PLL is popularly adopted by many recent research papers on VSC grid integration dynamic analysis for its simplicity, e.g., [5], [15]–[17].

On the other hand, PLL has many different structures. For example, in [18], the PI control block in SRF-PLL is replaced by a lead/lag unit so it can provide a better harmonic filtering performance. In 2003, Jovcic designed a new PLL

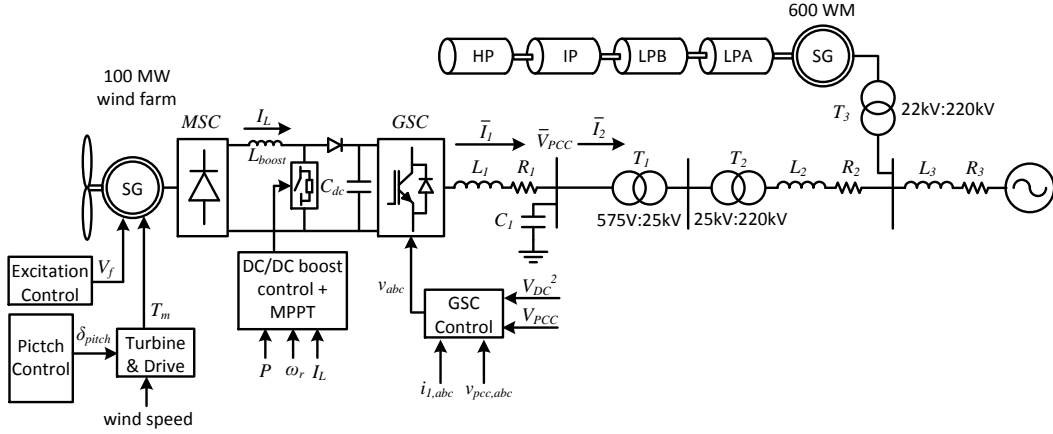


Fig. 1: MATLAB/SimPowerSystems Testbed: a 100 MW type-4 wind farm is connected to a grid through a long transmission line. A 600 MW steam turbine generator is also connected to the grid.

with three control blocks to estimate voltage magnitude, phase angle, and frequency, respectively [19]. Inside control blocks, a module named Harmonic Cancellation generates second order harmonic to mitigate unbalance effect. In addition, multiple low-pass filters are used to filter out higher order harmonics. Rodriguez *et al* designed a double second-order generalized integrator (DSOGI-PLL) to detect positive-sequence voltage [20]. The quadrature-signal generator (QSG) is used to filter out second harmonics in positive-sequence voltage. In [21], SRF-PLL based on decoupled double synchronous reference frames (DDSRF-PLL) is proposed and tested. It is not possible to examine every type of PLL structure on system stability. Hence, one other PLL structure, the lead/lag PLL proposed in [18] will be compared with SRF-PLL in this paper.

Our Contributions: Relying on small-signal analysis based on analytical models, we offer a reasonable explanation of the real-world phenomena: Why oscillations with significant different frequencies happened in wind farms with weak grid interconnections. This is achieved through dynamic modeling and linear system analysis. This paper is the first of the kind that indicates there are two oscillation modes associated with type-4 wind in weak grids. Both modes are sensitive to grid strength. The critical factor that determines which mode is dominant is identified. The analysis results are validated through a testbed with more comprehensive dynamics. Torsional interaction with a synchronous generator can be successfully demonstrated.

Organization: The rest of the paper is organized as follows. Section II presents the dynamic model. Section III presents eigenvalue analysis and dynamic simulation results based on the analytical models. In Section III, we present critical factors that causes difference in oscillation frequency. Section IV presents simulation results based on MATLAB/SimPowerSystems testbed. Torsional interaction with a synchronous generator is demonstrated. Section V concludes the paper.

II. ANALYTICAL MODEL

A complete type-4 wind model includes grid-side converter (GSC), PLL, dc-link dynamics, machine-side converter (MSC)

and synchronous generator (SG) dynamics [1]. The topology of a type-4 wind farm connected to the grid is shown in Fig. 2. L_1, R_1 are the RL filter parameters. C_1 denotes the shunt capacitor for reactive power compensation. R_g and L_g represent the aggregated resistances and inductances of the transformers and transmission lines. For grid dynamic studies, machine dynamics and MSC control are usually ignored [22]. Therefore, the analytical model will ignore machine dynamics and MSC control. Further, an entire wind farm is represented by a single wind turbine as shown in Fig. 2. This is due to the fact that a wind farm usually consists of same type wind turbines.

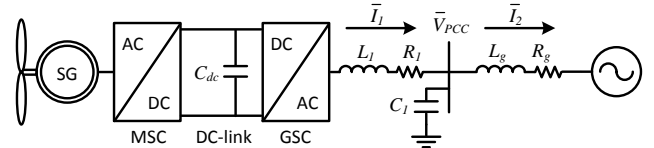


Fig. 2: A type-4 wind farm with grid interconnection.

The following subsections will introduce the dynamic model including dc-link, converter vector control, PLL, and grid. The block diagram of the dynamic model is shown in Fig. 3. In the dynamic model, there are two dq reference frames: converter-based and grid-based dq -frames. The converter reference frame has its d -axis aligned with the PCC voltage space vector, while the grid reference frame has its d -axis aligned with the grid voltage space vector. Superscript c notates the converter reference frame while superscript g notates the grid reference frame.

A. DC link

With the MSC and SG dynamics ignored, we assume the generator output power is constant and notated as P_{wind} . The relation between the dc-link voltage V_{dc} and the GSC power delivered to the grid P is shown in (1) and its per unitized version is shown in (2).

$$\frac{C_{dc}}{2} \frac{dV_{dc}^2}{dt} = P_{wind} - P \quad (1)$$

$$\underbrace{\frac{C_{dc} V_{dc,base}^2}{2P_{base}}}_{\tau} \frac{d(V_{dc}^{pu})^2}{dt} = P_{wind}^{pu} - P^{pu} \quad (2)$$

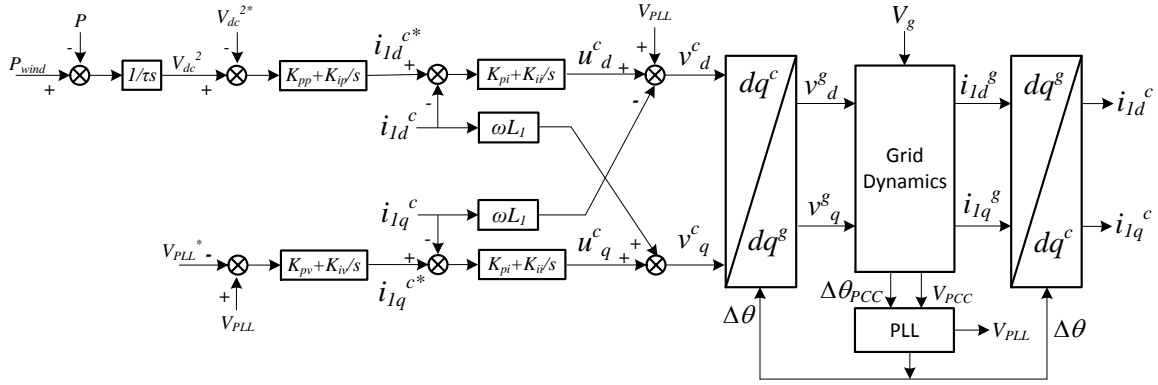


Fig. 3: Block diagram for the dynamic system model.

Superscript “pu” notates per unit variables. The parameter τ (0.0272 seconds) is computed based on the parameters of a 2 MW type-4 wind from MATLAB/SimPowerSystems: nominal dc link voltage 1100 V, capacitor size 0.09 F. Hereafter, the dc-link dynamics is expressed in per unit only. The superscript “pu” will be dropped.

B. Vector Control

A typical vector control [23] based on the converter reference frame is adopted for GSC with V_{dc}^2 control for the d -axis control and the PCC voltage control for the q -axis control. The control is based on the converter reference frame. The outer loops generates dq -current orders: i_{1d}^{c*} and i_{1q}^{c*} . From the inner current loop, the GSC voltage orders v_d^c and v_q^c are generated.

C. PLL

PLL uses the PCC bus three-phase voltage as input and outputs the PCC bus voltage magnitude, frequency and an angle. PLL is used to synchronize the converter with the grid. In this research, we adopt a simple second-order SRF-PLL. The details can be found in [24] and the control blocks are shown in Fig. 4. After the abc/dq block with θ as the input angle, the PCC voltage is in the converter dq -frame:

$$V_{PCC} e^{j(\theta_{PCC} - \theta)} = V_{PCC} e^{j(\Delta\theta_{PCC} - \Delta\theta)} = (v_{PCC,d}^c + jv_{PCC,q}^c),$$

where θ_{PCC} is the angle of the PCC voltage space vector, $\Delta\theta_{PCC} = \theta_{PCC} - \omega_0 t$ and V_{PCC} is the magnitude of the PCC voltage.

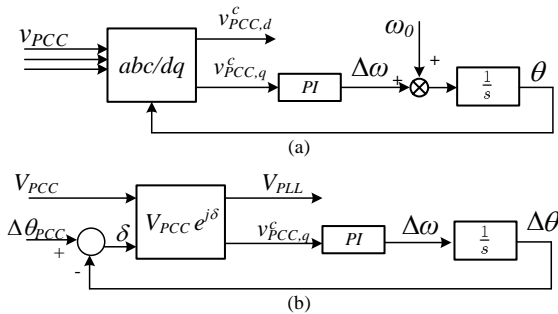


Fig. 4: Block diagrams of a PLL. (a) Original PLL; (b) PLL in dq -frames. (b) will be used in Fig. 3.

$v_{PCC,q}^c$ is fed into a proportional integral (PI) control block to generate the frequency deviation $\Delta\omega$. Integrating the frequency deviation results in $\Delta\theta$. Since the input of a PI

controller will be zero at steady-state, this control guarantees that $v_{PCC,q}^c$ becomes 0 at steady-state. Or, the d -axis of the converter frame is aligned with the PCC voltage space vector.

D. Grid dynamics

The inputs of the grid dynamic block are the GSC voltages in the grid reference frame. The outputs are also in the grid reference frame, including six dynamic states: converter currents i_{1d}^g, i_{1q}^g , grid currents i_{2d}^g, i_{2q}^g , and PCC voltages $v_{PCC,d}^g, v_{PCC,q}^g$. In addition, power P delivered from the GSC to the grid, PCC voltage magnitude V_{PCC} and angle $\Delta\theta_{PCC}$ can be found. The converter current can be further converted into the converter reference frame and fed into the vector control.

The grid dynamics include the shunt capacitor dynamics and the two series inductors' dynamics. Hence, there are three states in the complex domain \bar{I}_1, \bar{I}_2 and \bar{V}_{PCC} or six states in the real domain: $i_{1d}^g, i_{1q}^g, i_{2d}^g, i_{2q}^g, v_{PCC,d}^g$, and $v_{PCC,q}^g$.

$$\begin{cases} \frac{di_{1d}^g}{dt} = \frac{1}{L_1} (v_d^g - v_{PCC,d}^g - R_1 i_{1d}^g + \omega_0 L_1 i_{1q}^g) \\ \frac{di_{1q}^g}{dt} = \frac{1}{L_1} (v_q^g - v_{PCC,q}^g - R_1 i_{1q}^g - \omega_0 L_1 i_{1d}^g) \\ \frac{di_{2d}^g}{dt} = \frac{1}{L_g} (v_{PCC,d}^g - V_g - R_g i_{2d}^g + \omega_0 L_g i_{2q}^g) \\ \frac{di_{2q}^g}{dt} = \frac{1}{L_g} (v_{PCC,q}^g - 0 - R_g i_{2q}^g - \omega_0 L_g i_{2d}^g) \\ \frac{dv_{PCC,d}^g}{dt} = \frac{1}{C_1} (i_{1d}^g - i_{2d}^g + \omega_0 C_1 v_{PCC,q}^g) \\ \frac{dv_{PCC,q}^g}{dt} = \frac{1}{C_1} (i_{1q}^g - i_{2q}^g - \omega_0 C_1 v_{PCC,d}^g) \end{cases} \quad (3)$$

where ω_0 is nominal frequency (377 rad/s for 60 Hz ac system). L_g and R_g are the total inductance and resistance including those of the transmission lines and the transformers: $L_g = L_{T1} + L_{T2} + L_2 + L_3$ and $R_g = R_{T1} + R_{T2} + R_2 + R_3$.

III. ANALYSIS BASED ON THE DYNAMIC MODEL

The dynamic system shown in Fig. 3 is modeled in MATLAB/Simulink and parameters are given in Table I.

The steady-state values for states at a certain operating condition can be computed using algebraic calculation. With every state being assigned an initial value, flat run will be obtained for the dynamic system simulation without any imposed dynamic event. The nonlinear system can be linearized at an operating condition. This step can be achieved using MATLAB function `linmod`. In this section, a steady-state computing

TABLE I: Parameters of Simulink Model

Parameters	Values (in pu if not specified)
Power level	$P = 0.9$
Nominal frequency	$\omega_0 = 377 \text{ rad/s}$
Converter filter	$X_1 = 0.15, R_1 = 0.003, y_{c1} = 0.25$
Transformer (T1)	$X_{T1} = 0.02, R_{T1} = 0.002$
Transformer (T2)	$X_{T1} = 0.03, R_{T1} = 0.003$
Long transmission line	$X_2 = 0.3 \text{ to } 0.7, R_2 = 0.03 \text{ to } 0.07$
Short transmission line	$X_3 = 0.01, R_3 = 0.001$
DC time constant	$\tau = 0.0272 \text{ s}$
Current control	$K_{pi} = 0.4758, K_{ii} = 3.28$
Power control	$K_{pp} = 1.1, K_{ip} = 137.5$
Voltage control	$K_{pv} = 0.25, K_{iv} = 25$
PLL (13 Hz)	$K_{pPLL} = 60, K_{iPLL} = 1400$
PLL (34 Hz)	$K_{pPLL} = 60, K_{iPLL} = 18200$
PLL (30 Hz)	$K_{pPLL} = 100, K_{iPLL} = 10000$
PLL (60 Hz)	$K_{pPLL} = 314, K_{iPLL} = 24700$

procedure to find initial values will be presented. Following this subsection, eigenvalue analysis and time-domain simulation will be used to identify and confirm the low-frequency mode and the subsynchronous-frequency mode. Effect of PLL bandwidth on stability will be discussed. Then, participation factor analysis results will be presented to relate dynamic states to those modes. Finally, influence of PLL structure on system stability is examined.

A. Initialization

For flat run, the initial values should be assigned for each state variable in the MATLAB/Simulink model. A tutorial on Simulink-based dynamic model building can be found in [24] Chapter 2. The model shown in Fig. 3 has 13 state variables.

- 1 state variable is related to dc-link capacitor: V_{dc}^2 .
- 2 state variables are related to the PI controllers in the outer loop: x_1 and x_2 with their initial values as i_{1d}^c, i_{1q}^c .
- 2 state variables are related to the PI controllers in the inner loop: x_3 and x_4 with their initial values as u_d^c, u_q^c .
- 2 state variables are related to one PI controller and one integrator in the PLL respectively: $\Delta\omega, \Delta\theta$.
- 6 state variables are related to the grid dynamics: $i_{1d}^g, i_{1q}^g, i_{2d}^g, i_{2q}^g, v_{PCC,d}^g, v_{PCC,q}^g$.

The steady-state value for V_{dc}^2 is 1 pu. The steady-state value for $\Delta\omega$ is 0 and $\Delta\theta$ should be the same as the PCC voltage phase angle $\Delta\theta_{PCC}$. For all the rest initial values, we need to first carry out power flow analysis to find the PCC voltage angle $\Delta\theta_{PCC}$.

According to the system network topology in Fig. 2, the nodal admittance matrix \mathbf{Y} is formed as follows with the PCC bus notated as Bus 1 and the grid notated as Bus 2.

$$\mathbf{Y} = \begin{bmatrix} Y_{11} & Y_{12} \\ Y_{21} & Y_{22} \end{bmatrix} = \begin{bmatrix} \frac{1}{z_g} + y_c & -\frac{1}{z_g} \\ -\frac{1}{z_g} & \frac{1}{z_g} \end{bmatrix} \quad (4)$$

where $z_g = R_g + jX_g$ and $y_c = j\omega_0 C_1$. \mathbf{Y} matrix is separated into the real part and imaginary part, $\mathbf{G} = \text{Real}\{\mathbf{Y}\}$ and $\mathbf{B} = \text{Imag}\{\mathbf{Y}\}$.

The real power delivered to the grid P_{PCC} and the voltage magnitude at the PCC bus V_{PCC} are assumed to be known. For the grid voltage V_g , the voltage magnitude and phase angle are assumed as 1 pu and 0° . Hence, the only one unknown

variable is the voltage angle at the PCC bus $\Delta\theta_{PCC}$. It can be obtained using Newton Raphson (NR) method to solve the following AC power flow equation.

$$P_{PCC} = V_{PCC}^2 G_{11} + V_{PCC} V_g (G_{12} \cos \Delta\theta_{PCC} + B_{12} \sin \Delta\theta_{PCC})$$

After the PCC voltage phase angle $\Delta\theta_{PCC}$ is found, the dq -axis PCC voltages in the grid reference frame can be found. Similarly, the converter current $\bar{I}_1 = i_{1d}^g + j i_{1q}^g$ and the transmission line current $\bar{I}_2 = i_{2d}^g + j i_{2q}^g$ can all be found. Thus, the six states related to the grid dynamics can be found.

We may continue circuit analysis. Based on the PCC voltage and the converter current, the converter voltage can be found: v_d^g and v_q^g . Further, it is easy to convert the grid-frame variables into the converter-frame variables:

$$v_d^c + j v_q^c = (v_d^g + j v_q^g) e^{-j\Delta\theta_{PCC}}.$$

Converting the converter current from the grid frame to the converter frame, we may find the initial values for the two states related to the outer loop controls x_1 and x_2 .

Finally, we are able to find the initial values of the two inner loop controls x_3 and x_4 . The initial value of x_3 is u_d^c and the initial value of x_4 is u_q^c . From Fig. 3, $u_d^c = v_d^c - v_{PCC,d}^c + \omega L_1 i_{1d}^c$ and $u_q^c = v_q^c - v_{PCC,q}^c - \omega L_1 i_{1q}^c$. At steady-state, $v_{PCC,d}^c = V_{PCC}$ and $v_{PCC,q}^c = 0$ since the converter frame's d -axis is aligned with the PCC voltage.

Thus, we find all initial values for the 13 states.

B. Eigenvalue Loci

To examine the effect of PLL on the oscillation frequency, we test four PLLs in the dynamic model respectively. The Bode plots of the closed-loop PLL transfer function are shown in Fig. 5. Their parameters are listed in Table I. The strength of the grid can be represented by the short-circuit ratio (SCR) which is based on the per unit impedance of the transmission line when the power base is the nominal power of the wind generator ($\text{SCR} \approx \frac{1}{X_g}$).

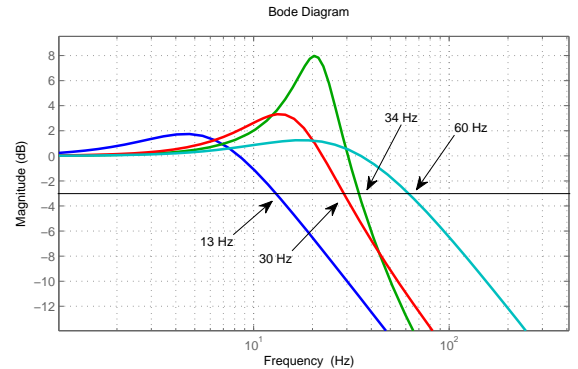


Fig. 5: Four PLL with different bandwidth: 13 Hz, 30 Hz, 34 Hz and 60 Hz.

Table II lists the eigenvalues for two cases. Case 1: $X_2 = 0.60$ for the 13 Hz PLL and Case 2: $X_2 = 0.46$ for the 34 Hz PLL case. They are the marginal conditions for these two PLLs. The dominant modes are bold for each case. With 13 Hz PLL, $\lambda_{8,9}$ indicate the dominant low-frequency oscillation at 5.02 Hz. With 34 Hz PLL, the modes $\lambda_{6,7}$ are the dominant eigenvalues and the oscillation frequency is 23.8 Hz.

TABLE II: Modes for different PLL bandwidths under marginal conditions

Mode	13 Hz PLL	34 Hz PLL
λ_1	-1174	-1172
$\lambda_{2,3}$	$-507.6 \pm j2\pi \times 337.6$	$-477.8 \pm j2\pi \times 347.4$
$\lambda_{4,5}$	$-52.5 \pm j2\pi \times 151.2$	$-52.9 \pm j2\pi \times 167.0$
$\lambda_{6,7}$	$-49.2 \pm j2\pi \times 22.28$	$-0.4 \pm j2\pi \times \mathbf{23.8}$
$\lambda_{8,9}$	$-0.3 \pm j2\pi \times \mathbf{5.02}$	$-8.0 \pm j2\pi \times 9.44$
λ_{10}	-97.3	-224.3
$\lambda_{11,12}$	$-17.4 \pm j2\pi \times 1.10$	$-34.3 \pm j2\pi \times 0.08$
λ_{13}	-34.5	-16.7

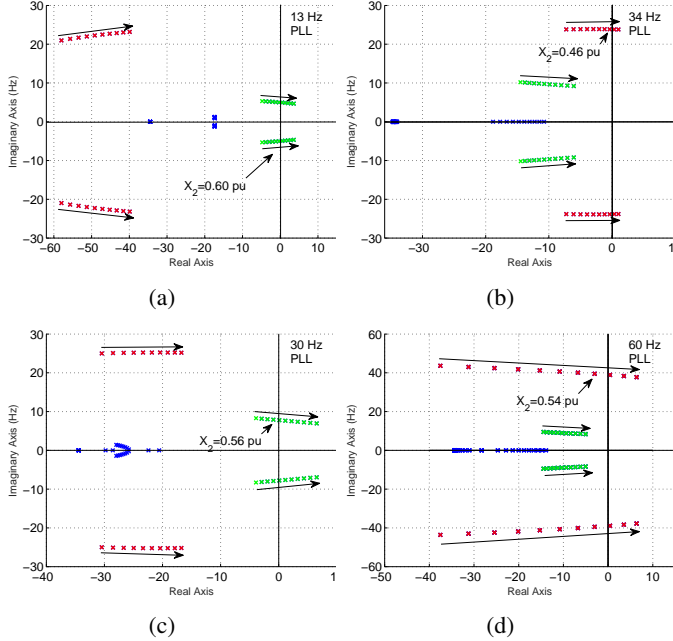


Fig. 6: Eigenvalue loci for SRF-PLL with different bandwidth. For each PLL, ten operating conditions are presented. (6a) (6c): X_2 changes from 0.5 to 0.7. (6b) X_2 changes from 0.3 to 0.5. (6d) X_2 changes from 0.4 to 0.6. Green ones notate low-frequency mode while red ones notate subsynchronous-frequency mode.

To analyze the system stability with different SCR, X_2 is increased until the system becomes unstable. The increment of X_2 is 0.02 pu. After each increment, the eigenvalues of the system are plotted. The eigenvalue loci are presented in Fig. 6. It can be clearly seen that the system has two oscillation modes sensitive to grid strength. One has a frequency lower than 10 Hz and is termed as the low-frequency oscillation mode, while the other has a frequency above 20 Hz and will be termed as the subsynchronous-frequency mode.

When the grid strength decreases, both modes move to the right half plane (RHP). Most notably, with different PLL parameters, different mode will appear dominant. When the PLL bandwidth is as low as 13 Hz, the low-frequency oscillation mode is dominant as demonstrated in Fig. 6a. When the PLL bandwidth is 60 Hz, the subsynchronous-frequency mode is dominant as demonstrated in Fig. 6d. What is more, a lower PLL bandwidth is better for stability. Shown in Fig. 6a, the marginal X_2 is 0.60 pu for a slow PLL. While the value is less than 0.56 pu for a faster PLL with 60 Hz bandwidth.

When the bandwidths are similar at ~ 30 Hz, it is found that if the second-order closed-loop PLL transfer function has less damping, then the subsynchronous-frequency mode will

be dominant for the PLL with 34 Hz bandwidth. See Fig. 6b. On the other hand, for the 30 Hz PLL with more damping, it is the low-frequency oscillation mode that is dominant as shown in Fig. 6c.

It can be found that the subsynchronous-frequency mode moves to the RHP when PLL's bandwidth increases. Further, this mode is very sensitive to the gain of the PLL integrator K_{iPLL} .

C. Time-domain Simulation Results

The dynamic model based on Fig. 3 is used to produce time-domain simulation results. The marginal stable conditions for the system are selected to calculate initial values ($X_2 = 0.60$ pu for the 13 Hz PLL case and $X_2 = 0.46$ pu for the 34 Hz PLL case). A small disturbance of 0.01 pu, is applied on V_{PLL} reference at 1 second. The step responses of V_{PCC} for the two cases are plotted in Fig. 7. It is observed that the oscillation frequency is 5 Hz for the 13 Hz PLL case and the oscillation frequency is about 23 Hz for the 34 Hz PLL case. The time-domain simulation results verify the linear analysis results.

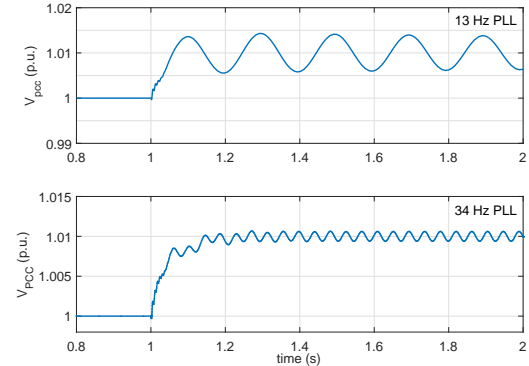


Fig. 7: Step responses of V_{PCC} show 5 Hz oscillations for 13 Hz PLL and 23 Hz oscillations for 34 Hz PLL.

D. Participation Factors

To determine which states are most relevant to the low-frequency and subsynchronous-frequency oscillation modes, participation factors related to each eigenvalue in Table II are calculated. Table III lists the participation factors for the subsynchronous mode $\lambda_{6,7}$ and the low-frequency mode $\lambda_{8,9}$. The high participation factors are marked as bold.

Based on the two cases (PLL bandwidths being 13 Hz or 34 Hz), we find that the subsynchronous mode $\lambda_{6,7}$ is related to dc-link dynamics, dc-link voltage control, and PLL. When PLL bandwidth is low, the low-frequency oscillation mode $\lambda_{8,9}$ is related to PLL and the ac voltage control (x_2). This finding concurs with the findings by ERCOT [25] and other papers in the literature, e.g., [1], [26].

When PLL bandwidth is high, it is found that both low-frequency and subsynchronous-frequency modes are related to dc-link dynamics, dc-link voltage control, and PLL.

TABLE III: Participation factors under marginal conditions

States	13 Hz PLL		34 Hz PLL	
	$\lambda_{6,7}$	$\lambda_{8,9}$	$\lambda_{6,7}$	$\lambda_{8,9}$
V_{dc}^2	0.3427	0.0926	0.1934	0.4157
i_{1d}^g	0.1031	0.0006	0.0457	0.0077
i_{1q}^g	0.0404	0.0077	0.0360	0.0106
i_{2d}^g	0.1145	0.0039	0.0653	0.0349
i_{2q}^g	0.2350	0.0345	0.2217	0.0223
$v_{PCC,d}^g$	0.0406	0.0053	0.0276	0.0017
$v_{pcc,q}^g$	0.0229	0.0017	0.0101	0.0046
θ	0.2297	0.3464	0.3979	0.1463
$\Delta\omega$	0.0377	0.2072	0.3571	0.1474
x_1	0.2692	0.0900	0.1240	0.3963
x_2	0.0479	0.2129	0.0165	0.0501
x_3	0.0119	0.0012	0.0059	0.0095
x_4	0.0948	0.1446	0.0320	0.0450

E. Comparison with Lead/lag PLL

In this subsection, PLL structure influence on stability is examined. The lead/lag PLL proposed in [18] is compared with SRF-PLL. Control structure of lead/lag PLL is presented in Fig. 8 and two lead/lag PLLs are designed to match the bandwidth of SRF-PLL, 13 Hz and 34 Hz. The bandwidth comparison is shown in Fig. 9.

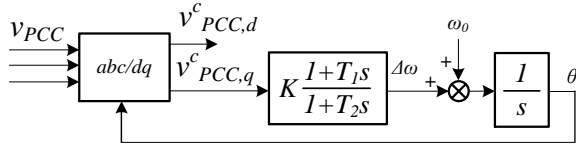


Fig. 8: Structure of a lead/lag PLL. Lead/lag 1 (bandwidth 13 Hz): $T_1 = 0.0037, T_2 = 0.0232, K = 91$; lead/lag 2 (bandwidth 34 Hz): $T_1 = 0.0013, T_2 = 0.0232, K = 457$.

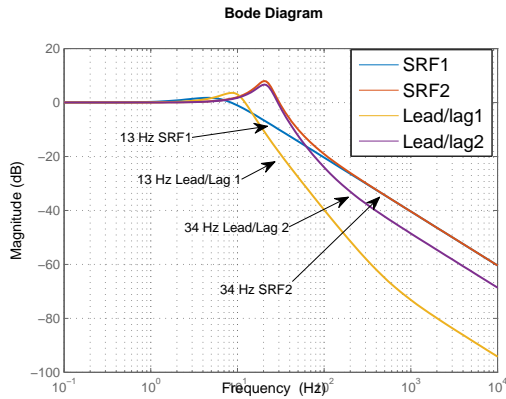


Fig. 9: Bandwidth comparison between SRF-PLL and lead/lag PLL.

The eigenvalue loci for the lead/lag PLLs are shown in Fig. 10. Compared with Fig. 6, we can find that the lead/lag PLL makes the system more stable. The 13 Hz lead/lag PLL increases the marginal X_2 from 0.6 to 0.64 pu while the 34 Hz lead/lag PLL increases the marginal X_2 from 0.46 to 0.54 pu.

The better performance is validated by the time-domain simulation results. Fig. 11 shows the dynamic responses corresponding to 13 Hz lead/lag PLL and SRF-PLL. At 5 s, X_2 was increased from 0.4 pu to 0.61 pu. 5 Hz oscillations appear

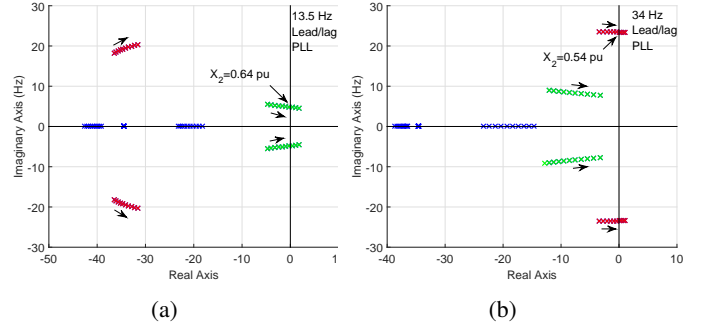


Fig. 10: Eigenvalue loci for lead/lag PLL with two different bandwidths. (10a) 13.5 Hz lead/lag PLL: X_2 changes from 0.5 to 0.7. (10b) 34 Hz lead/lag PLL: X_2 changes from 0.4 to 0.6.

in the system with SRF-PLL while the system with lead/lag PLL is stable.

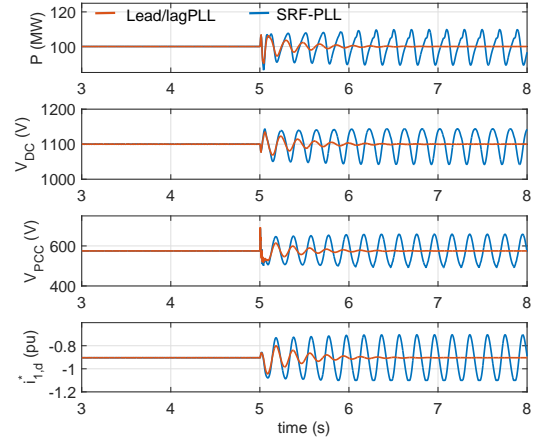


Fig. 11: Time domain simulation results comparison of lead/lag PLL versus SRF-PLL. Dynamic event: X_2 increases from 0.4 to 0.61 pu.

IV. VALIDATION IN MATLAB/SIMPOWERSYSTEMS

A testbed with both wind and a synchronous generator is built in MATLAB/SimPowerSystems. The topology of the testbed is shown in Fig. 1. The testbed is developed from the demo system of a 10 MW type-4 wind farm consisting of five 2 MW wind turbines connected to a 25 kV distribution system and delivering power to a 120 kV grid. Its control systems are based on the General Electric (GE) type-4 wind turbine generic model [27]. The parameters of the 2 MW synchronous generator are listed in Table VI while the parameters of the wind farm are listed in Table V.

In this paper, a 100 MW type-4 wind farm consisting of fifty 2 MW wind turbines is delivering power to a 220 kV grid. Two transformers are used to boost the voltage level from 575 V to 25 kV and from 25 kV to 220 kV. The PCC bus is connected to the grid through a long transmission line. A 22 kV 600 MW steam turbine and governor (TG) system is connected close to the grid.

The 600 MW synchronous generator model is from a demo system in MATLAB/SimPowerSystems related to steam turbine. The parameters of the 600 MW synchronous machine are from [28] and listed in Table VI. The generator turbine

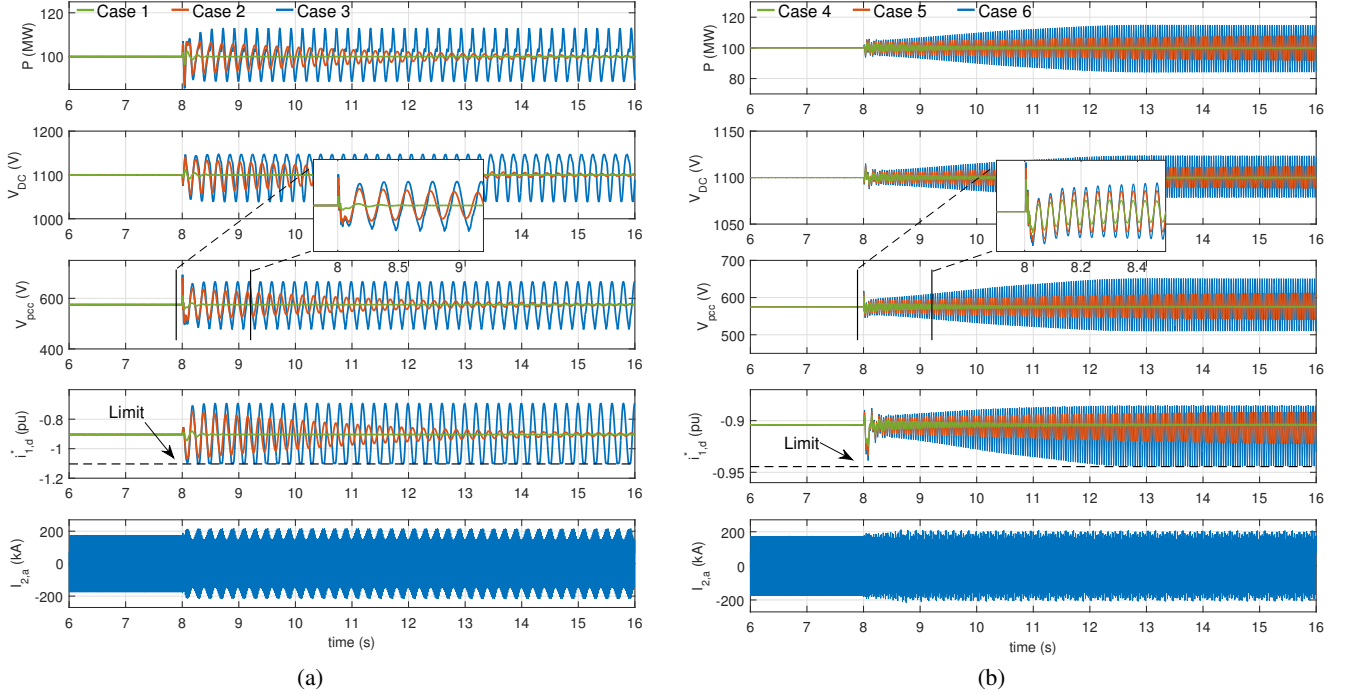


Fig. 12: The dynamic responses of type-4 wind farm. (a) 13 Hz PLL; (b) 34 Hz PLL.

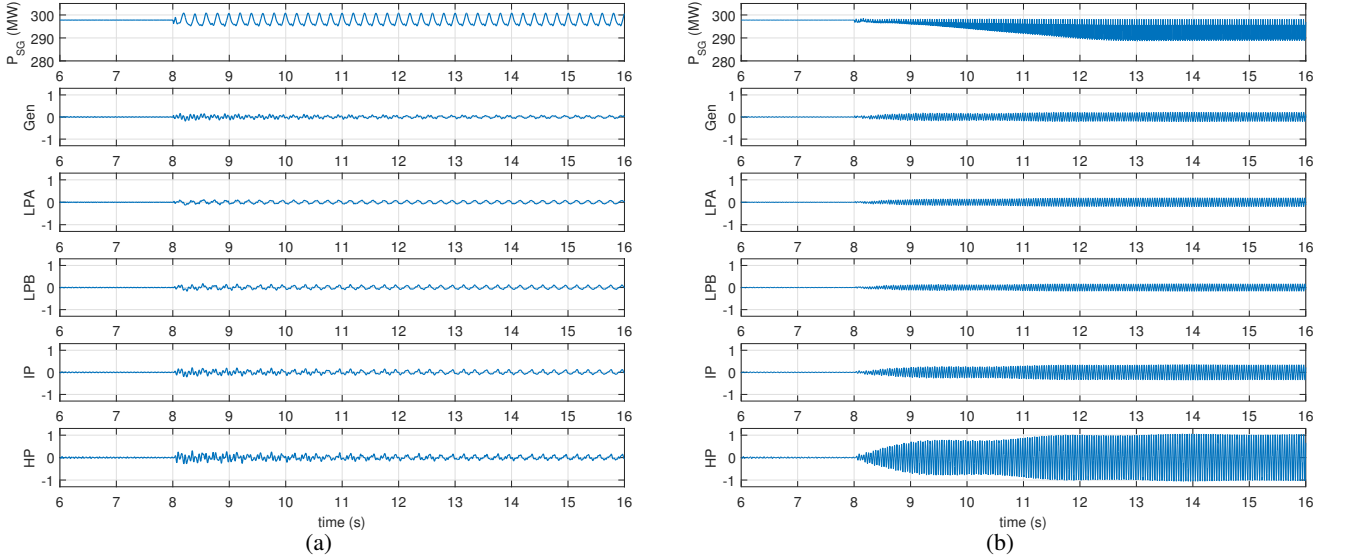


Fig. 13: The dynamic responses of the steam turbine governor. The lower ten plots are related to speed deviations in rad/s. (a) 13 Hz PLL, Case 3; (b) 34 Hz PLL, Case 6.

has only two turbine rotors: a low-pressure turbine rotor and a high-pressure turbine rotor. In this work, we adopted a more comprehensive shaft model with four turbine rotors. In our testbed, besides the generator rotor, the TG has four turbine rotors: two low-pressure turbine rotors (LPA and LPB), an intermediate-pressure turbine rotor (IP), and a high-pressure turbine rotor (HP). Hence, the steam TG has four torsional modes which are listed in Table VI. The parameters of each rotor are from Chapter 15 in [29]. Note that one torsional mode has a frequency of 24 Hz. This is very close to the 23.7 Hz oscillation in the wind with weak grid interconnection assuming that the PLL bandwidth is 34 Hz. In this case

study, we will demonstrate torsional interactions when the subsynchronous-frequency mode becomes dominant.

The dynamic events are assumed to be transmission line tripping. We assume that $R_2 + jX_2$ is the equivalent impedance of the long transmission path consisting of parallel transmission lines. Tripping one parallel transmission line will cause the increase of the impedance. Two SRF-PLLs are used for the tests: the one with 13 Hz bandwidth and the one with 34 Hz bandwidth. For each PLL, three line tripping cases are examined to show the impact of grid strength on dynamics. Total six cases have been studied and are listed as follows.

The initial value of X_2 is 0.4 pu.

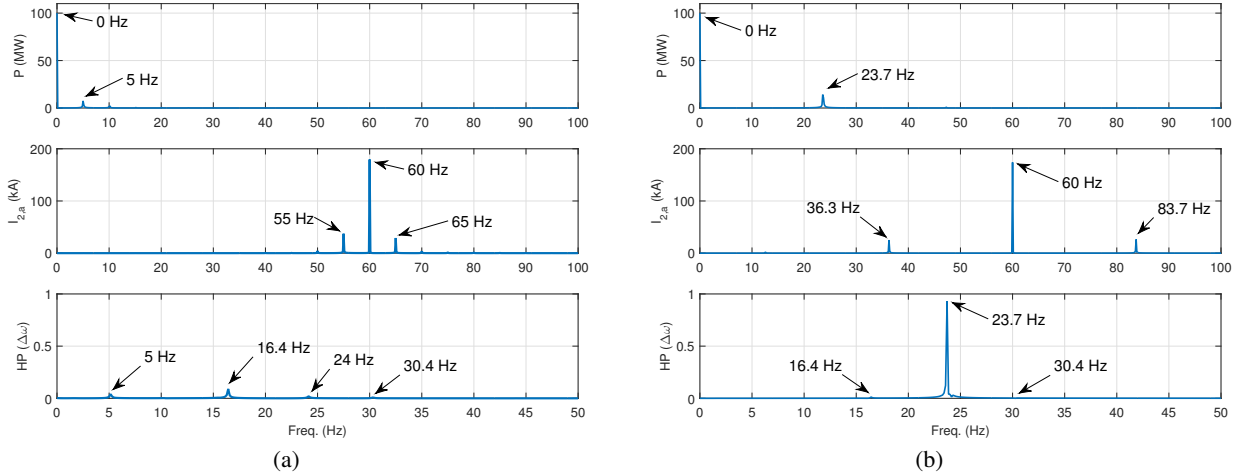


Fig. 14: FFT analysis for wind power P , AC current $I_{2,a}$, and $\Delta\omega$ of high-pressure rotor. (a) 13 Hz PLL, Case 3; (b) 34 Hz PLL, Case 6.

- Case 1 (13 Hz PLL): X_2 is increased to 0.46 pu.
- Case 2 (13 Hz PLL): X_2 is increased to 0.58 pu.
- Case 3 (13 Hz PLL): X_2 is increased to 0.61 pu.
- Case 4 (34 Hz PLL): X_2 is increased to 0.44 pu.
- Case 5 (34 Hz PLL): X_2 is increased to 0.46 pu.
- Case 6 (34 Hz PLL): X_2 is increased to 0.48 pu.

Fig. 12 presents the dynamic responses of wind farm variables and phase- a current from the PCC bus to the grid. The wind farm variables include the real power delivered from the PCC bus, dc-link voltage, PCC voltage, and d -axis current order. Fig. 13 presents the dynamic responses of the synchronous generator variables, including real power and speed deviations of the generator rotor, LPA, LPB, IP and HP. Fig. 14 presents the fast Fourier transformation (FFT) results for the wind power, phase- a current, and the speed deviation of HP based on a time window of data from 9 seconds to 16 seconds.

The left column presents the dynamic responses and FFT corresponding to the 13 Hz PLL cases. The right column presents the dynamic responses and FFT corresponding to the 34 Hz PLL cases.

Fig. 12a shows that for 13 Hz PLL, low-frequency oscillation mode is dominant. Fig. 14a indicates that the wind power has a 5 Hz oscillation. This 5 Hz is reflected as 55 Hz and 65 Hz harmonics in the phase- a current. The 5 Hz also appears in the synchronous generator output power and speed deviations of the generator rotor and TG rotors. Note that the HP rotor speed deviation also reflects the other torsional modes at 16.4 Hz, 24 Hz and 30.4 Hz.

Fig. 12b shows that for 34 Hz PLL, subsynchronous-frequency oscillation mode is dominant. Fig. 14b's FFT analysis indicates that the wind power has a 23.7 Hz oscillation. This 23.7 Hz oscillation is reflected as 36.3 Hz and 86.7 Hz harmonics in the phase- a current. The 23.7 Hz oscillation mode interacts with the 24 Hz torsional mode. FFT analysis of the speed deviation of HP shows a very large component of 23.7 Hz. This is a clear evidence of torsional interaction. Further, comparing Fig. 13 left column and right column, we see that the synchronous generator power has a 4 MW peak to peak oscillations for the 13 Hz PLL while 10 MW peak to peak oscillations appear for the 34 Hz PLL case. The speed

deviation of HP shows more obvious torsional interaction. For the 34 Hz PLL case, the peak to peak magnitude of the oscillation reaches 2 rad/s. Compared with the severe oscillation, the oscillations in the HP speed deviation for the 13 Hz PLL case are negligible.

Remarks: The testbed successfully demonstrates the low-frequency oscillations and the subsynchronous oscillations in type-4 wind with weak grid interconnection. The significant difference in oscillation frequency is due to the different PLL parameters. Further, the case study successfully demonstrates that if the subsynchronous-frequency mode has a frequency close to a torsional mode of a remote synchronous generator, torsional interaction happens.

V. CONCLUSION

In this paper, the mechanism of low-frequency oscillations and subsynchronous oscillations in type-4 wind with weak grid interconnection is revealed. Compared to the research in the literature, this is the first kind to investigate two distinctive oscillation modes observed in real world. A dynamic model is built to demonstrate both modes. Both modes will move to the RHP when the grid strength reduces. Depending on the parameters of PLL, one mode will be dominant. This paper reveals the relation of PLL parameters to these two modes. Case study also demonstrates the potential torsional interaction that can occur on a remote synchronous generator.

APPENDIX

REFERENCES

- [1] N. P. Strachan and D. Jovicic, "Stability of a variable-speed permanent magnet wind generator with weak ac grids," *IEEE Transactions on Power Delivery*, vol. 25, no. 4, pp. 2779–2788, 2010.
- [2] Y. Zhou, D. Nguyen, P. Kjaer, and S. Saylor, "Connecting wind power plant with weak grid-challenges and solutions," in *Power and Energy Society General Meeting (PES), 2013 IEEE*. IEEE, 2013, pp. 1–7.
- [3] J. Hu, Y. Huang, D. Wang, H. Yuan, and X. Yuan, "Modeling of grid-connected dfig-based wind turbines for dc-link voltage stability analysis," *IEEE Transactions on Sustainable Energy*, vol. 6, no. 4, pp. 1325–1336, 2015.
- [4] J. Z. Zhou, H. Ding, S. Fan, Y. Zhang, and A. M. Gole, "Impact of short-circuit ratio and phase-locked-loop parameters on the small-signal behavior of a vsc-hvdc converter," *IEEE Transactions on Power Delivery*, vol. 29, no. 5, pp. 2287–2296, 2014.

TABLE IV: Parameters of type-4 wind turbine

Parameter	Value (SI)
Rated real power	2 MW
DC-link voltage	1100 V
Rated voltage	575 V
Nominal frequency	60 Hz
X_d, X'_d, X''_d	313 m Ω , 71.0 m Ω , 60.5 m Ω
X_q, X'_q, X''_q	114 m Ω , 58.3 m Ω
R_s, X_l	1.44 m Ω , 40.8 m Ω
T'_{do}, T''_{do}	4.49 s, 0.0681 s
T'_{qo}, T''_{qo}	0.0513 s
Inertial, friction factor	0.62 s, 0.01
poles	2
L_{boost}	1.2 mH
C_{dc}	90 mF
L_1, R_1, C_1	0.06 mH, 0.45 m Ω , 3.6 mF

TABLE V: Parameters of type-4 wind farm

Parameter	Value (SI)
Number of WT	50
Rated power	100 MW
Nominal frequency	60 Hz
L_{T1}, R_{T1}	0.30 mH, 11.3 m Ω
Rated voltage	220 kV
L_{T2}, R_{T2}	23.1 mH, 0.87 Ω
L_2, R_2	462 to 705 mH, 17.4 to 26.6 Ω
L_3, R_3	11.6 mH, 0.44 Ω

TABLE VI: Parameters of Steam Turbine and Governor

Parameter	Value (SI)
Rated power	600 MW
Power level	300 MW
Rated voltage	22 kV
Nominal frequency	60 Hz
X_d, X'_d, X''_d	1.33 Ω , 0.20 Ω , 0.16 Ω
X_q, X'_q, X''_q	1.28 Ω , 0.37 Ω , 0.16 Ω
X_l	0.11 Ω
T'_{do}, T''_{do}	4.5 s, 0.04 s
T'_{qo}, T''_{qo}	0.67 s, 0.09 s
Inertial, poles	0.855 s, 2
Torsional Mode 1	16.3 Hz
Torsional Mode 2	24.1 Hz
Torsional Mode 3	30.3 Hz
Torsional Mode 4	44.0 Hz
L_{T3}, R_{T3}	25.7 mH, 4.84 Ω

- [5] J. Hu, B. Wang, W. Wang, H. Tang, Y. Chi, and Q. Hu, "Small signal dynamics of dfig-based wind turbines during riding through symmetrical faults in weak ac grid," *IEEE Transactions on Energy Conversion*, vol. 32, no. 2, pp. 720–730, 2017.
- [6] M. Zhao, X. Yuan, J. Hu, and Y. Yan, "Voltage dynamics of current control time-scale in a vsc-connected weak grid," *IEEE Transactions on Power Systems*, vol. 31, no. 4, pp. 2925–2937, 2016.
- [7] H. Yuan, X. Yuan, and J. Hu, "Modeling of grid-connected vscs for power system small-signal stability analysis in dc-link voltage control timescale," *IEEE Transactions on Power Systems*, 2017.
- [8] Y. Huang and D. Wang, "Effect of control loops interactions on power stability limits of vsc with integrated to ac system," *IEEE Transactions on Power Delivery*, 2017.
- [9] S. H. Huang, J. Schmall, J. Conto, J. Adams, Y. Zhang, and C. Carter, "Voltage control challenges on weak grids with high penetration of wind generation: Ercot experience," in *2012 IEEE Power and Energy Society General Meeting*, July 2012, pp. 1–7.
- [10] H. Liu, X. Xie, J. He, T. Xu, Z. Yu, C. Wang, and C. Zhang, "Subsynchronous interaction between direct-drive PMSG based wind farms and weak ac networks," *IEEE Transactions on Power Systems*, vol. 32, no. 6, pp. 4708–4720, 2017.
- [11] L. Papangelis, M.-S. Debry, T. Prevost, P. Panciatici, and T. Van Cutsem, "Stability of a voltage source converter subject to decrease of short-circuit capacity: a case study," *Proceedings of the 20th PSCC*, 2017.
- [12] K. M. Alawasa, Y. A.-R. I. Mohamed, and W. Xu, "Modeling, analysis, and suppression of the impact of full-scale wind-power converters on

subsynchronous damping," *IEEE Systems Journal*, vol. 7, no. 4, pp. 700–712, 2013.

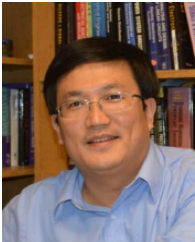
- [13] L. Fan, "Modeling type-4 wind in weak grids," *IEEE Transactions on Sustainable Energy*, vol. 10, no. 2, pp. 853–864, April 2019.
- [14] L. Fan and Z. Miao, "Wind in weak grids: 4 hz or 30 hz oscillations?" *IEEE Transactions on Power Systems*, vol. 33, no. 5, pp. 5803–5804, Sep. 2018.
- [15] J. Hu, Q. Hu, B. Wang, H. Tang, and Y. Chi, "Small signal instability of pll-synchronized type-4 wind turbines connected to high-impedance ac grid during lvr," *IEEE Transactions on Energy Conversion*, vol. 31, no. 4, pp. 1676–1687, 2016.
- [16] H. Yuan, X. Yuan, and J. Hu, "Modeling of grid-connected vscs for power system small-signal stability analysis in dc-link voltage control timescale," *IEEE Transactions on Power Systems*, vol. 32, no. 5, pp. 3981–3991, Sep. 2017.
- [17] W. He, X. Yuan, and J. Hu, "Inertia provision and estimation of pll-based dfig wind turbines," *IEEE Transactions on Power Systems*, vol. 32, no. 1, pp. 510–521, Jan 2017.
- [18] C. Zhan, C. Fitzer, V. K. Ramachandaramurthy, A. Arulampalam, M. Barnes, and N. Jenkins, "Software phase-locked loop applied to dynamic voltage restorer (dvr)," in *2001 IEEE Power Engineering Society Winter Meeting. Conference Proceedings (Cat. No.01CH37194)*, vol. 3, Jan 2001, pp. 1033–1038 vol.3.
- [19] D. Jovicic, "Phase locked loop system for facts," *IEEE Transactions on Power Systems*, vol. 18, no. 3, pp. 1116–1124, Aug 2003.
- [20] P. Rodriguez, R. Teodorescu, I. Candela, A. V. Timbus, M. Liserre, and F. Blaabjerg, "New positive-sequence voltage detector for grid synchronization of power converters under faulty grid conditions," in *2006 37th IEEE Power Electronics Specialists Conference*, June 2006, pp. 1–7.
- [21] P. Rodriguez, J. Pou, J. Bergas, J. I. Candela, R. P. Burgos, and D. Boroyevich, "Decoupled double synchronous reference frame pll for power converters control," *IEEE Transactions on Power Electronics*, vol. 22, no. 2, pp. 584–592, March 2007.
- [22] Y. Zhou, D. D. Nguyen, P. C. Kjr, and S. Saylor, "Connecting wind power plant with weak grid - challenges and solutions," in *2013 IEEE Power Energy Society General Meeting*, July 2013, pp. 1–7.
- [23] A. Yazdani and R. Iravani, *Voltage-sourced converters in power systems: modeling, control, and applications*. John Wiley & Sons, 2010.
- [24] L. Fan, *Control and Dynamics in Power Systems and Microgrids*. CRC Press, 2017.
- [25] S.-H. Huang, J. Schmall, J. Conto, J. Adams, Y. Zhang, and C. Carter, "Voltage control challenges on weak grids with high penetration of wind generation: Ercot experience," in *Power and Energy Society General Meeting, 2012 IEEE*. IEEE, 2012, pp. 1–7.
- [26] L. Fan and Z. Miao, "An explanation of oscillations due to wind power plants weak grid interconnection," *IEEE trans. Sustainable Energy*, vol. 9, no. 1, pp. 488–490, Jan 2018.
- [27] N. W. Miller, J. J. Sanchez-Gasca, W. W. Price, and R. W. Delmerico, "Dynamic modeling of ge 1.5 and 3.6 mw wind turbine-generators for stability simulations," in *Power Engineering Society General Meeting, 2003, IEEE*, vol. 3. IEEE, 2003, pp. 1977–1983.
- [28] IEEE SSR working group and others, "Second benchmark model for computer simulation of subsynchronous resonance," *IEEE Trans. on Power Apparatus and Systems*, vol. 104, no. 5, pp. 1057–1066, 1995.
- [29] P. Kundur, *Power System Stability And Control*, ser. EPRI power system engineering series. McGraw-Hill, 1994. [Online]. Available: https://books.google.com/books?id=v3RrXh_GkwmsC



Yin Li (S'13) received the B.S. degree in electrical engineering from University of South Florida (USF) in May 2014 and joined the USF Smart Grid Power Systems Lab in Aug. 2014 for Ph.D. study. He works on converter penetrated system modeling and control.



Lingling Fan (SM'08) received the B.S. and M.S. degrees in electrical engineering from Southeast University, Nanjing, China, in 1994 and 1997, respectively, and the Ph.D. degree in electrical engineering from West Virginia University, Morgantown, in 2001. Currently, she is an Associate Professor with the University of South Florida, Tampa, where she has been since 2009. She was a Senior Engineer in the Transmission Asset Management Department, Midwest ISO, St. Paul, MN, from 2001 to 2007, and an Assistant Professor with North Dakota State University, Fargo, from 2007 to 2009. Her research interests include power systems and power electronics. Dr. Fan serves an editor for IEEE Trans. Sustainable Energy and IEEE Trans. Energy Conversion.



Zhixin Miao (SM'09) received the B.S.E.E. degree from the Huazhong University of Science and Technology, Wuhan, China, in 1992, the M.S.E.E. degree from the Graduate School, Nanjing Automation Research Institute (Nanjing, China) in 1997, and the Ph.D. degree in electrical engineering from West Virginia University, Morgantown, in 2002.

Currently, he is with the University of South Florida (USF), Tampa. Prior to joining USF in 2009, he was with the Transmission Asset Management Department with Midwest ISO, St. Paul, MN, from 2002 to 2009. His research interests include power system stability, microgrid, and renewable energy.